

Unexpectedly Strong Auger Recombination in Halide Perovskites

Jimmy-Xuan Shen, Xie Zhang,* Suvadip Das, Emmanouil Kioupakis, and Chris G. Van de Walle*

The emergence of halide perovskites for photovoltaic applications has triggered great interest in these materials for solid-state light emission. Higher order electron–hole recombination processes can critically affect the efficiency of such devices. In the present work, the Auger recombination coefficients are computed in the prototypical halide perovskite, $\text{CH}_3\text{NH}_3\text{PbI}_3$ (MAPbI₃), using first-principles calculations. It is demonstrated that Auger recombination is responsible for the exceptionally high third-order recombination coefficient observed in experiment. The large Auger coefficient is attributed to a coincidental resonance between the bandgap and interband transitions to a complex of higher-lying conduction bands. Additionally, it is found that the distortions of PbI₆ octahedra contribute significantly to the high Auger coefficient, offering potential avenues for materials design.


1. Introduction

Halide perovskites comprise a group of materials with the chemical formula ABX_3 , in which the A-site cation is either a metallic element or an organic molecule, the B-site is occupied by a metallic element and X is a halogen anion such as I^- , Br^- , and Cl^- . Methylammonium lead iodide (MAPbI₃, MA = CH_3NH_3)^[1] is the archetypal member of this family, where the A-site molecule (MA^+) sits in a lattice of PbI₆ octahedra (see **Figure 1**). These materials have attracted widespread attention as candidates for affordable and efficient photovoltaics; within a few years reported power conversion efficiencies have risen from 3% to over 20%,^[2–4] and a worldwide effort to improve the conversion efficiency of these materials is still underway.

Dr. J.-X. Shen
Department of Physics
University of California
Santa Barbara, CA 93106-9530, USA

Dr. X. Zhang, Prof. C. G. Van de Walle
Materials Department
University of California
Santa Barbara, CA 93106-5050, USA
E-mail: xiezhang@ucsb.edu; vandewalle@mrl.ucsb.edu

Dr. S. Das, Prof. E. Kioupakis
Department of Materials Science and Engineering
University of Michigan
Ann Arbor, MI 48109, USA

 The ORCID identification number(s) for the author(s) of this article can be found under <https://doi.org/10.1002/aenm.201801027>.

DOI: 10.1002/aenm.201801027

Given the high solar conversion efficiency, detailed balance in the Shockley–Queisser formulation suggests that radiative recombination will be efficient.^[5] Halide perovskites should therefore also make good light emitters and light-emitting diodes (LEDs) have indeed been fabricated^[6] and have been shown to cover the entire visible spectrum.^[7] However, the operation of LEDs requires much higher carrier densities (typically around 10^{18} cm^{-3})^[8] compared to photovoltaics, where the carrier density is fundamentally limited by the availability of solar radiation. At these higher carrier densities, nonradiative recombination mechanisms might play a much more important role

than in solar cells. The prospect of making efficient LEDs based on halide perovskites thus hinges on the behavior of carrier recombination at higher carrier densities.

Higher order recombination processes play an important role in determining the quantum efficiency of an LED. Under typical LED operating conditions, the nonequilibrium densities of electrons (n) and holes (p) can be assumed to be equal. The internal quantum efficiency (IQE) is then described by

$$\text{IQE} = \frac{k_2 n^2}{k_1 n + k_2 n^2 + k_3 n^3} \quad (1)$$

where k_1 , k_2 , and k_3 represent the mono-, bi-, and trimolecular recombination coefficients, respectively. For MAPbI₃, peak IQEs of greater than 70% have been achieved.^[6,9] The IQE peaks around $n = 10^{18} \text{ cm}^{-3}$ and falls off rapidly as carrier density increases; the fall-off is due to the trimolecular recombination dominating at higher carrier densities. Transient spectroscopy^[10–12] and photoluminescence^[9,13] measurements have obtained trimolecular recombination coefficients ranging from 5.4×10^{-29} to $1.6 \times 10^{-28} \text{ cm}^6 \text{ s}^{-1}$. While strategies to mitigate the efficiency fall-off via device design have shown promise,^[14] a fundamental understanding of the underlying recombination mechanism and additional avenues for materials design are still needed.

In this paper we set out to determine from first principles whether Auger recombination can explain the observed efficiency loss at high carrier densities. Auger is a trimolecular process in which the energy released by electron–hole recombination promotes a third charge carrier to an excited state. This process is nonradiative, as the excess energy of the excited

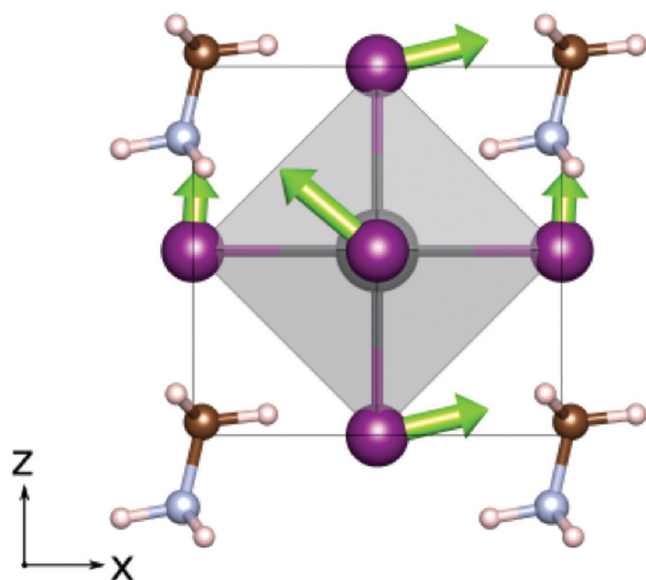


Figure 1. Twelve-atom unit cell of MAPbI₃ where the I atoms are at the ideal face-center positions. The arrows indicate displacement of the I atoms upon relaxation within a cubic cell shape. For clarity the length of the displacement vector is enhanced by a factor of five.

carrier is lost to phonons. If that third charge carrier is an electron, the Auger process is called an electron–electron–hole (eeh) process; in case it is a hole, it is called a hole–hole–electron (hhe) process.

All of the traditional semiconductors with bandgaps higher than 1 eV exhibit Auger coefficients C around $10^{-30} \text{ cm}^6 \text{ s}^{-1}$.^[15] The measured k_3 coefficients in MAPbI₃ are two orders of magnitude higher than the Auger coefficients C in other materials with similar bandgaps,^[15] prompting the question whether Auger is actually the responsible mechanism. Other mechanisms (such as carrier leakage) can lead to large k_3 values, as illustrated by investigations on the more widely studied nitride-based LEDs.^[16] Our first-principles calculations allow us to examine whether the Auger process is really so much stronger than in traditional semiconductors, and what the underlying mechanisms are.

We use first-principles methods (Section 2) to compute the Auger recombination coefficient in MAPbI₃ and investigate its relationship with key features in the band structure. We find that the unexpectedly high Auger coefficient in MAPbI₃ originates from unique features in its band structure induced by large spin–orbit coupling (SOC)^[17] (Section 3.1). We also find that k -space splitting of the band edges significantly enhances Auger recombination, and that this splitting is correlated with structural distortions (Section 3.2). It turns out that distortions can be engineered by strain or by alloying, resulting in a suppression of Auger recombination. In this spirit, we search for other perovskite iodides that minimize the degree of internal distortion, thus identifying promising candidates for higher-efficiency light emitters. Finally, we discuss how the Auger effect of MAPbI₃ compares with other common semiconductors (Section 3.3) and demonstrate that the experimentally observed third-order recombination coefficient is indeed due to Auger recombination.

2. Methodology

Fully ab initio calculations of Auger recombination rates have recently been developed and applied to III–V semiconductors.^[18] Our calculations of eigenvalues and wavefunctions are based on density functional theory (DFT)^[19,20] and norm-conserving pseudopotentials as implemented in the Quantum ESPRESSO package.^[21] A plane-wave energy cutoff of 100 Ry along with a $6 \times 6 \times 6$ k -point grid were used in the calculations of structure and charge density. We use the local density approximation (LDA) for the exchange–correlation functional. To account for the LDA underestimation of the bandgap, the conduction-band energies are shifted relative to the valence bands (commonly referred to as a scissors shift). The overall shape of the scissors-shifted band structure agrees well with the quasiparticle band structure^[22] at a fraction of the computational cost.

The large SOC and lack of inversion symmetry lead to non-collinear spins. The spin–orbit interactions are included via a perturbing Hamiltonian (ΔH_{SOC}) constructed using the vector part of the ab initio pseudopotentials.^[23] The corrections to the spin-degenerate eigenvalues are obtained by diagonalizing ΔH_{SOC} in the spin-degenerate basis. To ensure that the spinor wavefunctions can be represented as a linear combination of the spin-degenerate wavefunctions we included 40 unoccupied conduction bands in our band structure.

Each state in the band structure can be labeled by a general state index $\mathbf{I} \equiv [\mathbf{k}, m]$, where \mathbf{k} is the crystal momentum in reciprocal space and m is the band index. A $20 \times 20 \times 20$ k -space grid was used for the calculations of the Auger rates. The Auger rate is given by Fermi's golden rule^[18]

$$R_{\text{Auger}} = \frac{2\pi}{\hbar} \sum_{1234} f_1 f_2 (1 - f_3)(1 - f_4) |M_{1234}|^2 \delta(\epsilon_1 + \epsilon_2 - \epsilon_3 - \epsilon_4) \quad (2)$$

where $\mathbf{I} = 1, 2, 3, 4$ represent the four single-particle states involved in the Auger process, f_i are Fermi occupation factors, and the δ function enforces energy conservation. The matrix element M_{1234} is the antisymmetrized screened-Coulomb matrix element

$$\langle \psi_1 \psi_2 | \mathcal{W} | \psi_3 \psi_4 \rangle - \langle \psi_1 \psi_2 | \mathcal{W} | \psi_4 \psi_3 \rangle \quad (3)$$

computed from the single-particle wavefunctions ψ_i . If we assume equal densities of electrons and holes, we can define an Auger coefficient as $C = R_{\text{Auger}}/n^3$. The matrix elements are nonzero only if momentum is conserved (i.e., $\mathbf{k}_1 + \mathbf{k}_2 = \mathbf{k}_3 + \mathbf{k}_4$).

In our calculations of the Auger coefficients for the eeh (C_n) and hhe (C_p) processes, we treat the scissors-shifted bandgap as an adjustable parameter to model the effect of alloying MAPbI₃ with other materials and to better understand the interplay between the Auger coefficient and features in the band structure. Results for MAPbI₃ itself are obtained at the experimental bandgap value of 1.60 eV.^[24]

3. Results and Discussions

The low-temperature ground-state phase of MAPbI₃ is orthorhombic ($Pnma$), where the PbI₆ octahedra are

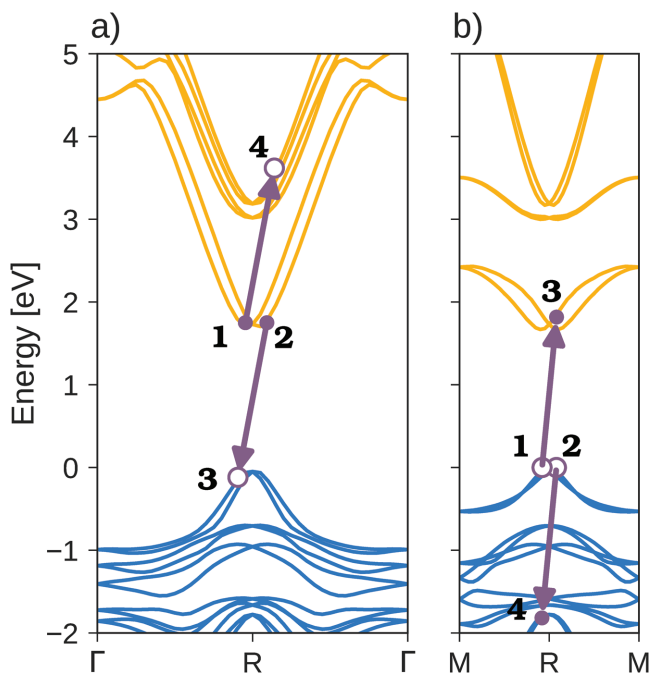


Figure 2. Band structure of MAPbI₃ including SOC, with the gap adjusted to the experimental value, plotted along the a) R → Γ and b) R → M directions. Auger recombination events for a) the eeh and b) hhe processes are indicated.

significantly tilted and deformed. At slightly above room temperature (327 K), MAPbI₃ undergoes a transition to the cubic phase (*Pm* $\bar{3}m$).^[25] In our simulations we focus on this cubic phase with a 12-atom unit cell. While the overall cell shape is cubic, atomic relaxation leads to significant deviations from the ideal perovskite positions (see Figure 1). Using the Pb atom as the reference point at the center of the cubic unit cell, we find that the three iodine atoms are displaced 0.28, 0.39, and 0.43 Å from their face-centered positions, and such internal distortions lead to an effective Rashba splitting,^[26] which significantly modifies the band structure near the band edges and breaks the spin degeneracy. This splitting can be observed in the band structure of the relaxed unit cell shown in Figure 2.

The states near the conduction-band minimum (CBM) have predominantly Pb-*p* character, and the valence-band maximum (VBM) states predominantly I-*p* character. When SOC is included, the six spin-degenerate bands near the CBM at *R* split into two bands at the band edge and four bands at 1.29 and 1.46 eV above the CBM, and the bandgap changes from a direct gap at *R* to a slightly indirect transition between states slightly off *R*. These key features of our band structure agree well with the quasiparticle band structure of Gao et al.^[22] The quasiparticle band structures of the orthorhombic^[27] and tetragonal^[28] phases have been calculated by other groups but the much larger computational

cost of studying Auger recombination in these larger-unit-cell phases is beyond our current capabilities.

We choose 10¹⁸ cm⁻³ as a typical carrier density for an LED. At this density, the initial states are restricted to the portion of the Brillouin zone near the band extrema around *R*. Since Auger recombination must conserve energy and momentum, the process will be strong if final states are available with energies approximately one bandgap away from the band edges. Such states (labeled as 4 in Figure 2) are clearly available in the MAPbI₃ band structure, for both the eeh and hhe processes.

At the experimental bandgap of 1.60 eV, we obtain Auger coefficients of $C_n = 2.7 \times 10^{-29}$ cm⁶ s⁻¹ and $C_p = 4.6 \times 10^{-29}$ cm⁶ s⁻¹. These values are two orders of magnitude larger than Auger coefficients in semiconductors with similar bandgaps.^[15] We now explore the physical mechanisms responsible for this enhancement.

3.1. Coincidental Resonance

For the hhe process, an array of valence bands is available that can serve as final states for Auger recombination, explaining the high C_p value (4.6×10^{-29} cm⁶ s⁻¹). For the eeh process, Figure 3b shows our calculated Auger coefficient as a function of bandgap. This plot is obtained by computing C_n as a function of the scissors-adjusted gap, while keeping the matrix elements in Equation (2) fixed. While changing the bandgap can be considered a rough approximation to alloying MAPbI₃ with other materials, simulation of alloys is not our primary goal. Our main focus is to elucidate the mechanisms responsible for the high Auger coefficient in this material. If Auger transitions are restricted to the first two conduction bands (CB1 and CB2) (see Figure 3a), the computed Auger coefficient falls off rapidly as a function of bandgap—a behavior similar to intraband eeh processes in conventional direct-gap semiconductors.^[29] If transitions to the higher-lying four bands (CB3–CB6) are included

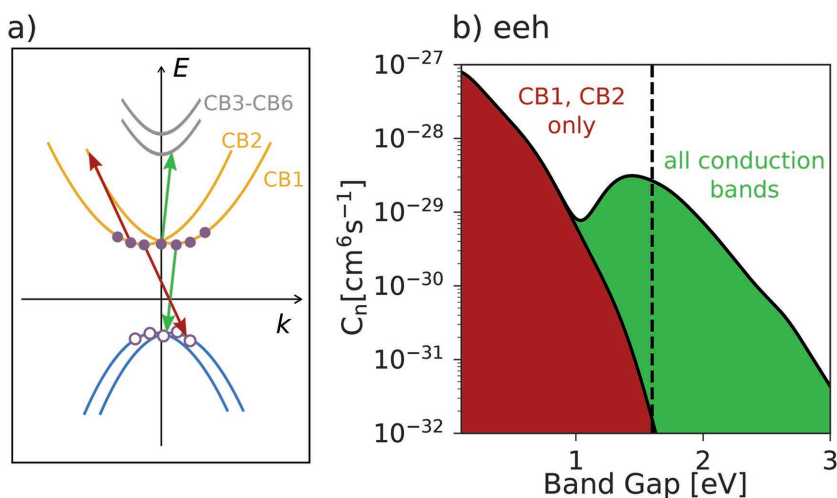


Figure 3. a) Schematic of Auger processes involving only the CB1 and CB2 bands versus processes with transitions to the CB3–CB6 bands. b) Computed Auger coefficients as a function of scissors-adjusted bandgap at a carrier density $n = 10^{18}$ cm⁻³, for processes restricted to CB1 and CB2 versus processes with transitions to all conduction bands. The dashed line represents the experimental bandgap of 1.60 eV.

the Auger coefficient is dramatically increased and shows a distinct maximum when the bandgap is equal to the energy difference between CB1 and CB2 and the higher-lying conduction bands (CB3–CB6) (Figure 3b); this happens to occur very close to the bandgap of MAPbI₃, where C_n is enhanced by three orders of magnitude relative to the case where transitions to the higher lying conduction bands would not occur. We conclude that most of the high eeh Auger recombination rate observed in MAPbI₃ can be attributed to the coincidental resonance of the bandgap with interband transitions to a complex of higher lying conduction bands. We note that a similar resonance was observed in InAs and has been a focus of band-structure engineering aimed at suppressing the Auger recombination.^[30]

3.2. Effects of Lattice Distortions on Auger

Spin–orbit coupling not only leads to the splitting of the conduction bands that results in the enhancement of the eeh Auger rate, but (in combination with a breaking of inversion symmetry) it also causes a splitting of states near the band extrema.^[31] We will see that this splitting also has a distinct effect on the Auger coefficients.

The CBM and VBM of MAPbI₃ are each comprised of two spinor states. When the PbI₆ octahedra are undistorted (by fixing the Pb atom at the center of the unit cell, and the iodine atoms at the ideal face-center positions), the bands at the CBM and VBM are degenerate. When the atoms are allowed to relax, the bands split into two bands. Most noticeably, the internal distortions lead to a linear- k splitting of the band edges, which directly influences the distribution of states involved in the Auger process.

A schematic of how the CBM changes due to structural distortion is shown in Figure 4. In the case of undistorted (ideal) Pb and I positions, the VBM and CBM are both at the high-symmetry R point. Structural relaxations lead to a linear- k splitting, which in turn results in a ring of states around R . The band edge of the relaxed structure has a higher dimensionality, and thus many more states available for the Auger process. Therefore, at the same carrier density, each of the states at the band edge for the relaxed structure will have a lower quasi-Fermi occupation factor than in the ideal structure. This is evident in the fact that the quasi-Fermi level is lower for electrons (and higher for holes) in the relaxed atomic configuration than in the ideal structure.

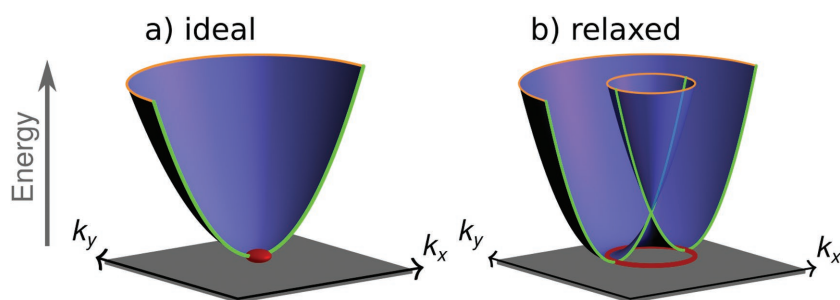


Figure 4. Schematic of the CBM energy dispersion of MAPbI₃ near the R point for a) the ideal and b) the relaxed structure. The band-edge states are shown in red.

Table 1. Quasi-Fermi level μ_F (referenced to the CBM/VBM) and extent of Brillouin-zone filling (% BZ) for electrons/holes, for ideal and relaxed atomic configurations of MAPbI₃. The sign of μ_F is positive in case of degenerate doping for electrons (Fermi level above the CBM) and negative in case of degenerate doping for holes (Fermi level below the VBM). The computed Auger coefficients ($C_{n/p}$) are also listed. All values are obtained for a carrier density of 10^{18} cm⁻³.

Carrier	Structure	μ_F [eV]	% BZ	$C_{n/p}$ [cm ⁶ s ⁻¹]
Electrons	Ideal	28.9	0.2	2.2×10^{-30}
	Relaxed	-15.7	0.6	2.7×10^{-29}
Holes	Ideal	-26.2	0.3	4.6×10^{-30}
	Relaxed	30.3	0.8	6.5×10^{-29}

To examine the distributions of band-edge states that participate in Auger recombination, we can compute the extent of the region in the Brillouin zone occupied by electrons or holes. Table 1 shows results for Brillouin-zone filling (% BZ) corresponding to a volume in which 99% of the electrons (holes) reside, for the case of a carrier density of 10^{18} cm⁻³. The table shows that in the ideal structure the charge carriers are much more concentrated near the R point, making it significantly harder to simultaneously satisfy energy and momentum conservation.

The Auger coefficients versus bandgap for the ideal and relaxed structures are shown in Figure 5. The Auger coefficient is clearly significantly lower for the ideal structure. The Auger coefficients at the experimental bandgap of 1.60 eV are listed in Table 1. The concentration of charge carriers near the R point causes the eeh Auger coefficient for the ideal structure to be 92% lower than in the relaxed structure; the hhe Auger coefficient experiences a similar drop, by 86%. These Auger coefficients for the ideal structure are close to the value of $\approx 10^{-30}$ cm⁶ s⁻¹ that seems to be a lower limit for Auger coefficients, as observed across a wide range of materials spanning a large range of bandgaps.^[15]

The connection between distortions and higher Auger coefficient is evident. Schemes for controlling the octahedral distortion have been proposed, such as using anisotropic strain^[32] or alloying with other halide perovskites.^[33] Atomic substitutions can of course have other effects on the band structure; still, looking for materials with lower internal distortions can be a useful criterion in the search for materials with lower Auger coefficients.

The degree of distortion of the perovskite octahedra can be characterized by the variance of the angles subtended by the bonds at the Pb atom^[34]

$$\sigma_{\theta(\text{oct})}^2 = \frac{1}{11} \sum_{i=1}^{12} (\theta_i - 90^\circ)^2 \quad (4)$$

We have computed the bond-angle variance $\sigma_{\theta(\text{oct})}^2$ for a number of inorganic and hybrid iodide perovskites. The results, shown in Figure 6, show a clear trend with the size of the cations: smaller distortions occur for larger A-site cations as well as for smaller B-site cations. A similar general trend is observed as a function of tolerance factor: the tolerance factor increases for larger A-site

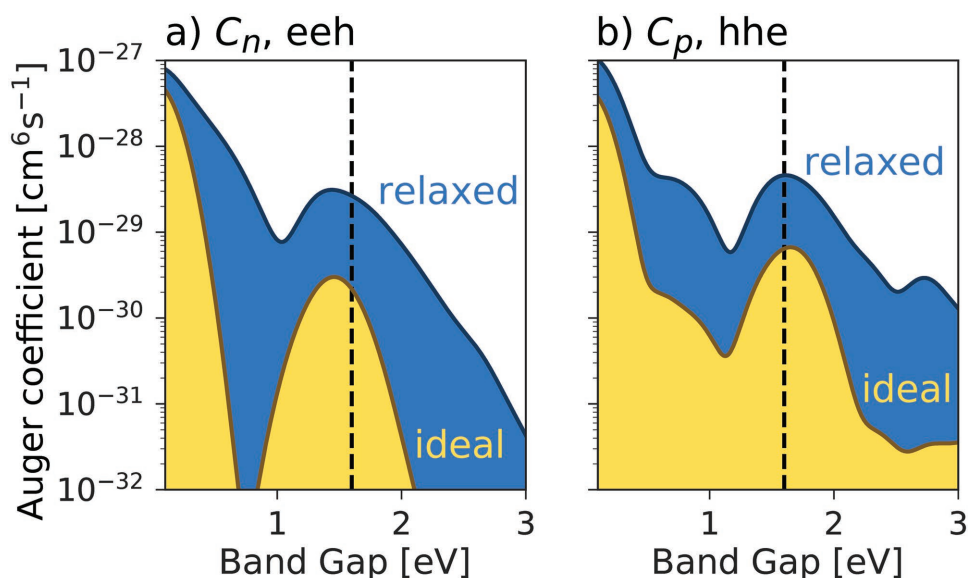


Figure 5. a) eeh and b) hhe Auger coefficients versus scissor-shifted bandgap for the ideal and relaxed structures.

cations as well as for smaller B-site cations, and materials with larger tolerance factors tend to have smaller distortions.^[35] We feel that the bond-angle variance provides a more direct measure of the distortions. A complete investigation of the distortion of different types of halide perovskites is beyond the scope of the present work. However, we note that the structural parameters of different halide perovskites can be obtained by simple calculations or from existing materials databases^[36] and can serve as a useful starting point for screening of promising light-emitting materials. The large range of octahedral distortions shown by the halide perovskites, as illustrated in Figure 6, allows for using the distortion as a tuning parameter in materials design.

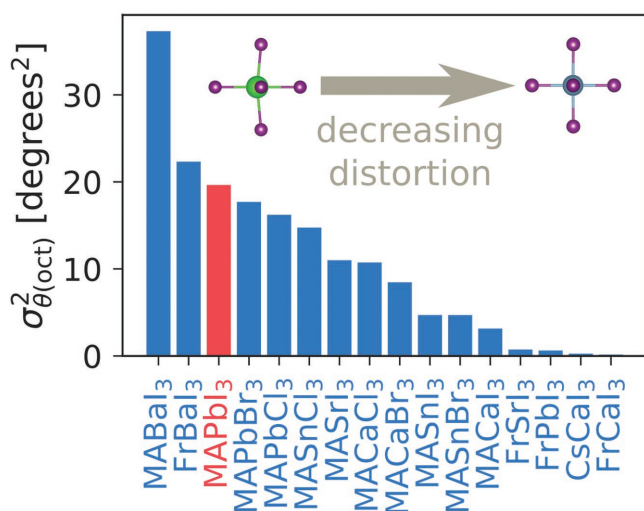


Figure 6. Bond-angle variance of several inorganic and hybrid halide perovskites. The calculations were done using LDA assuming the cubic phase.

3.3. Implications for Device Efficiency

We now discuss the impact of the Auger coefficient on the efficiency of LEDs. At the experimental bandgap of 1.60 eV, the combined Auger coefficient (eeh + hhe) from our calculations is $7.3 \times 10^{-29} \text{ cm}^6 \text{ s}^{-1}$ for the relaxed structure and $8.6 \times 10^{-30} \text{ cm}^6 \text{ s}^{-1}$ for the ideal structure. In Figure 7 we plot the IQE as a function of the carrier density n (Equation (1)) using our calculated Auger coefficient as k_3 . For the radiative recombination coefficient k_2 we use a calculated value of $8.4 \times 10^{-11} \text{ cm}^3 \text{ s}^{-1}$ ^[37] and for k_1 the value reported by Richter et al.^[9] We compare our results with an IQE curve calculated using experimentally determined recombination coefficients

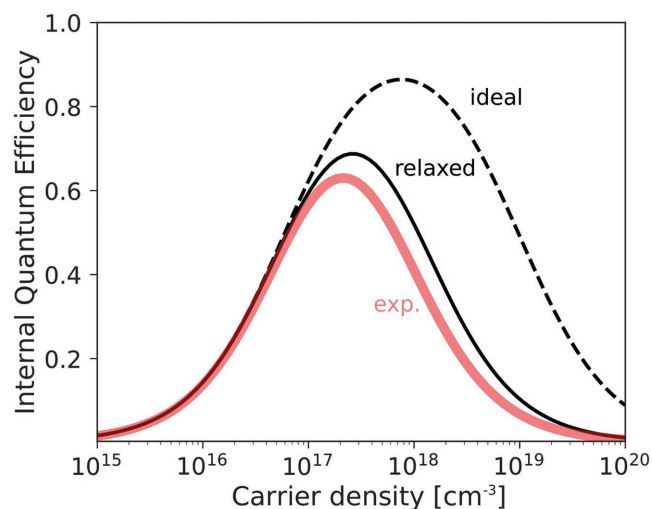


Figure 7. Internal quantum efficiency calculated as a function of carrier density (Equation (1)) using k_3 values corresponding to our calculated Auger coefficients for the relaxed (solid curve) and ideal (dashed black curve) perovskite structures, and compared to experimental values.

$k_1 = 5 \times 10^6 \text{ s}^{-1}$, $k_2 = 8.1 \times 10^{-11} \text{ cm}^3 \text{ s}^{-1}$, and $k_3 = 1.1 \times 10^{-28} \text{ cm}^6 \text{ s}^{-1}$, obtained in ref. [9] from fitting transient absorption measurements. In ref. [9] it was also demonstrated that this curve matched results from photoluminescence quantum yield measurements. The calculated and experimental IQE agree very well with each other, thus confirming that the third-order recombination observed in MAPbI₃ is primarily due to Auger recombination.

Figure 7 indicates that Auger recombination causes the IQE of MAPbI₃ to drop off above a carrier density of $2.5 \times 10^{17} \text{ cm}^{-3}$ and also reduces the peak IQE. Zou et al.^[14] fabricated LEDs from 2D layered perovskites and found that the efficiency fall-off occurs at lower carrier densities compared to the 3D perovskites. Auger recombination thus apparently plays an even more significant role for 2D perovskites. However, as discussed in Section 3.2 and Figure 5, Auger recombination can be dramatically reduced if lattice distortions are suppressed. This reduced Auger coefficient results in an IQE with a peak that increases from 69% to 86%, with the carrier density at peak efficiency shifting to $7.6 \times 10^{17} \text{ cm}^{-3}$ (Figure 7).

4. Conclusions

We have computed the Auger recombination coefficient of the prototypical halide perovskite, MAPbI₃. Our calculations result in a total Auger coefficient (eeh + hhe) of $7.3 \times 10^{-29} \text{ cm}^6 \text{ s}^{-1}$, in good agreement with the third-order recombination coefficients reported by experiments,^[10,11,13] confirming that Auger is the dominant loss mechanism in MAPbI₃ at high carrier concentrations.

The high Auger recombination coefficient for the eeh process is mainly due to the coincidental resonance of the bandgap with states that are roughly one bandgap away from the band edges. We also found that if the distortions in the metal-halide lattice are removed, Auger recombination can be dramatically suppressed. To aid future attempts at engineering this feature, we computed the octahedral distortions in a number of halide perovskites. In order for halide perovskites to reach quantum efficiencies comparable to those of traditional III–V semiconductor devices, materials will have to be identified that avoid the coincidental resonance that is present in MAPbI₃, and that minimize distortions of the metal-halide lattice.

Acknowledgements

J.-X.S. and X.Z. contributed equally to this work. This work was supported by the U. S. Department of Energy (DOE), Office of Science, Basic Energy Sciences, under Award No. DE-SC0010689. Computational resources were provided by the National Energy Research Scientific Computing Center, a DOE Office of Science User Facility supported by the Office of Science of the U. S. Department of Energy under Contract No. DE-AC0205CH11231.

Conflict of Interest

The authors declare no conflict of interest.

Keywords

Auger recombination, DFT calculations, halide perovskite, light-emitting diode

Received: April 3, 2018

Revised: August 21, 2018

Published online: September 19, 2018

- [1] Z. Xiao, R. A. Kerner, L. Zhao, N. L. Tran, K. M. Lee, T.-W. Koh, G. D. Scholes, B. P. Rand, *Nat. Photonics* **2017**, *11*, 108.
- [2] A. Kojima, K. Teshima, Y. Shirai, T. Miyasaka, *J. Am. Chem. Soc.* **2009**, *131*, 6050.
- [3] H. Zhou, Q. Chen, G. Li, S. Luo, T.-B. Song, H.-S. Duan, Z. Hong, J. You, Y. Liu, Y. Yang, *Science* **2014**, *345*, 542.
- [4] N. J. Jeon, J. H. Noh, W. S. Yang, Y. C. Kim, S. Ryu, J. Seo, S. I. Seok, *Nature* **2015**, *517*, 476.
- [5] O. D. Miller, E. Yablonovitch, S. R. Kurtz, *IEEE J. Photovoltaics* **2012**, *2*, 303.
- [6] S. D. Stranks, H. J. Snaith, *Nat. Nanotechnol.* **2015**, *10*, 391.
- [7] S. Adjokatse, H.-H. Fang, M. A. Loi, *Mater. Today* **2017**, *20*, 413.
- [8] S. P. DenBaars, *Solid State Luminescence*, Springer, Dordrecht, The Netherlands **1993**.
- [9] J. M. Richter, M. Abdi-Jalebi, A. Sadhanala, M. Tabachnyk, J. P. Rivett, L. M. Pazos-Outón, K. C. Gödel, M. Price, F. Deschler, R. H. Friend, *Nat. Commun.* **2016**, *7*, 13941.
- [10] J. Fu, Q. Xu, G. Han, B. Wu, C. H. A. Huan, M. L. Leek, T. C. Sum, *Nat. Commun.* **2017**, *8*, 1300.
- [11] C. Wehrenfennig, G. E. Eperon, M. B. Johnston, H. J. Snaith, L. M. Herz, *Adv. Mater.* **2014**, *26*, 1584.
- [12] Y. Yang, M. Yang, Z. Li, R. Crisp, K. Zhu, M. C. Beard, *J. Phys. Chem. Lett.* **2015**, *6*, 4688.
- [13] R. L. Milot, G. E. Eperon, H. J. Snaith, M. B. Johnston, L. M. Herz, *Adv. Funct. Mater.* **2015**, *25*, 6218.
- [14] W. Zou, R. Li, S. Zhang, Y. Liu, N. Wang, Y. Cao, Y. Miao, M. Xu, Q. Guo, D. Di, L. Zhang, C. Yi, F. Gao, R. H. Friend, J. Wang, W. Huang, *Nat. Commun.* **2018**, *9*, 608.
- [15] K. A. Bulashevich, S. Yu. Karpov, *Phys. Status Solidi C* **2008**, *5*, 2066.
- [16] J. Piprek, *Phys. Status Solidi A* **2010**, *207*, 2217.
- [17] J. Even, L. Pedesseau, J.-M. Jancu, C. Katan, *J. Phys. Chem. Lett.* **2013**, *4*, 2999.
- [18] E. Kioupakis, D. Steiauf, P. Rinke, K. T. Delaney, C. G. Van de Walle, *Phys. Rev. B* **2015**, *92*, 035207.
- [19] P. Hohenberg, W. Kohn, *Phys. Rev.* **1964**, *136*, B864.
- [20] W. Kohn, L. J. Sham, *Phys. Rev.* **1965**, *140*, A1133.
- [21] P. Giannozzi, S. Baroni, N. Bonini, M. Calandra, R. Car, C. Cavazzoni, D. Ceresoli, G. L. Chiarotti, M. Cococcioni, I. Dabo, A. Dal Corso, S. de Gironcoli, S. Fabris, G. Fratesi, R. Gebauer, U. Gerstmann, C. Gougoussis, A. Kokalj, M. Lazzeri, L. Martin-Samos, N. Marzari, F. Mauri, R. Mazzarello, S. Paolini, A. Pasquarello, L. Paulatto, C. Sbraccia, S. Scandolo, G. Sclauzero, A. P. Seitsonen, A. Smogunov, P. Umari, R. M. Wentzcovitch, *J. Phys.: Condens. Matter* **2009**, *21*, 395502.
- [22] W. Gao, X. Gao, T. A. Abtew, Y.-Y. Sun, S. Zhang, P. Zhang, *Phys. Rev. B* **2016**, *93*, 085202.
- [23] M. S. Hybertsen, S. G. Louie, *Phys. Rev. B* **1986**, *34*, 2920.
- [24] A. M. A. Leguy, P. Azarhoosh, M. I. Alonso, M. Campoy-Quiles, O. J. Weber, J. Yao, D. Bryant, M. T. Weller, J. Nelson, A. Walsh, M. van Schilfgaarde, P. R. F. Barnes, *Nanoscale* **2016**, *8*, 6317.
- [25] M. T. Weller, O. J. Weber, P. F. Henry, A. M. Di Pumpo, T. C. Hansen, *Chem. Commun.* **2015**, *51*, 4180.
- [26] X. Zhang, Q. Liu, J.-W. Luo, A. J. Freeman, A. Zunger, *Nat. Phys.* **2014**, *10*, 387.

- [27] M. R. Filip, C. Verdi, F. Giustino, *J. Phys. Chem. C* **2015**, *119*, 25209.
- [28] F. Brivio, K. T. Butler, A. Walsh, M. van Schilfgaarde, *Phys. Rev. B* **2014**, *89*, 155204.
- [29] D. Steiauf, E. Kioupakis, C. G. Van de Walle, *ACS Photonics* **2014**, *1*, 643.
- [30] I. P. Marko, Z. Batool, K. Hild, S. R. Jin, N. Hossain, T. J. C. Hosea, J. P. Petropoulos, Y. Zhong, P. B. Dongmo, J. M. O. Zide, S. J. Sweeney, *Appl. Phys. Lett.* **2012**, *101*, 221108.
- [31] M. Kepenekian, J. Even, *J. Phys. Chem. Lett.* **2017**, *8*, 3362.
- [32] L. Leppert, S. E. Reyes-Lillo, J. B. Neaton, *J. Phys. Chem. Lett.* **2016**, *7*, 3683.
- [33] J.-H. Lee, N. C. Bristowe, J. H. Lee, S.-H. Lee, P. D. Bristowe, A. K. Cheetham, H. M. Jang, *Chem. Mater.* **2016**, *28*, 4259.
- [34] K. Robinson, G. V. Gibbs, P. H. Ribbe, *Science* **1971**, *172*, 567.
- [35] V. M. Goldschmidt, *Naturwissenschaften* **1926**, *14*, 477.
- [36] A. Jain, S. P. Ong, G. Hautier, W. Chen, W. D. Richards, S. Dacek, S. Cholia, D. Gunter, D. Skinner, G. Ceder, K. A. Persson, *APL Mater.* **2013**, *1*, 011002.
- [37] X. Zhang, J.-X. Shen, W. Wang, C. G. Van de Walle, *ACS Energy Lett.* **2018**, *3*, 2329.